

# CO12-1 Profile measurements of Coherent Cherenkov Radiation Matched to the Circular Plane at KURNS-LINAC

N. Sei, T. Takahashi<sup>1</sup>

*Research Institute for Measurement and Analytical Instrumentation, National Institute of Advanced Industrial Science and Technology*

<sup>1</sup>*Institute for Integrated Radiation and Nuclear Science, Kyoto University*

**INTRODUCTION:** In order to generate an intense light beam in the terahertz (THz) region, we proposed coherent Cherenkov radiation matched to circular plane wave (CCR-MCP) using a hollow conical dielectric [1]. Cherenkov radiation concentrates on the surface of a cone with the Cherenkov angle [2]. Because it was difficult to converge the Cherenkov radiation, it was not used as a THz-wave source based on electron accelerators. In the scheme of the CCR-MCP, the CCR generated on the inner surface of the hollow conical dielectric is entirely reflected from the conical surface and the CCR phase is matched to the basal plane. Then, the CCR-MCP beam is easy to transport for applied experiments. We have already observed the CCR-MCP beam and measured its radiation power. In this fiscal year, we measured two-dimensional distributions of the CCR-MCP beam in the experimental room.

**EXPERIMENTS:** We performed the experiments of the CCR-MCP with an L-band linac at Kyoto University Institute for Integrated Radiation and Nuclear Science. High-density polyethylene was used as a material for the hollow conical dielectric. The observation of hollow structure peculiar to the CCR-MCP beam is easier as the inner diameter of the hollow conical dielectric is larger. However, the intensity of the CCR-MCP beam decreases as the inner diameter increase, and the inner diameter was set to be 10 mm. When the bottom of the hollow conical dielectric was small, the CCR-MCP beam was spread by diffraction at the experimental room. Therefore, the length of the hollow conical dielectric was set to be 80 mm, which was the maximum value that the CCR-MCP beam could be transported to the experimental room.

An aluminum collimator with the length of 150 mm and the inner diameter of 8 mm was set in front of the hollow conical dielectric so that the electron beam did not collide with the hollow conical dielectric. In order to avoid generation of coherent transition radiation, a kapton film with a thickness of 50  $\mu\text{m}$  was located at 0.4 m from the hollow conical dielectric and the electron beam and the CCR-MCP beam were separated by it. The CCR-MCP beam was transported to the experimental room and emitted from a monochromator without a diffraction grating to the air. This beam was converted into a parallel beam by a spherical concave mirror. It was focused by another spherical concave mirror and measured by a Si bolometer. We installed an aperture with a diame-

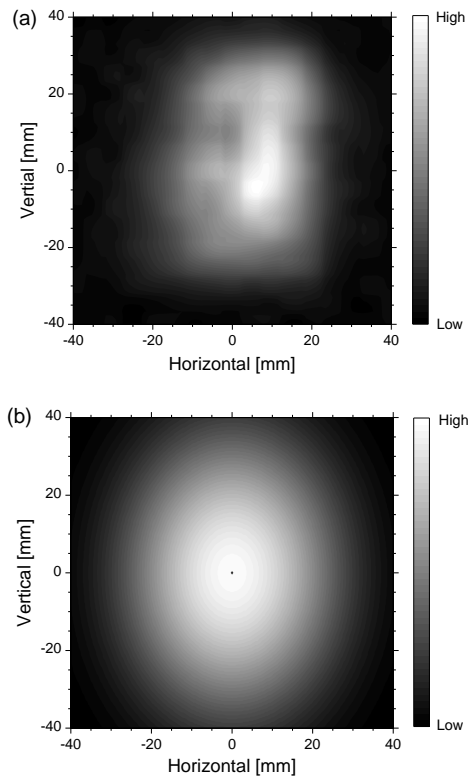


Fig. 1 Measured (a) and calculated (b) two-dimensional distributions of the CCR-MCP.

ter of 10 mm, which was set on an X-Y axis translation stage, at the parallel beam, and measured the two-dimensional distribution of the CCR-MCP beam.

**RESULTS:** The measured two-dimensional distribution of the CCR-MCP beam is shown in Fig. 1(a). It is noted that the hollow structure, which the radiator has, disappears at the observation point due to the diffraction. Because the short-focus concave mirror is used instead of a toroidal mirror to make a parallel beam, the profile of the CCR-MCP beam is an ellipse with the short axis in the horizontal direction. Fig. 1(b) shows the two-dimensional distribution of the CCR-MCP beam calculated for the hollow conical dielectric with the length of 80 mm. The measured standard deviations are about 20% smaller than the calculated ones. However, we note that both the measured profile and the calculated profile have a similar, shorter axis in the horizontal direction. We plan to measure the two-dimensional distribution of the CCR-MCP beam near the hollow conical dielectric.

## REFERENCES:

- [1] N. Sei *et al.*, Phys. Lett. A **379** (2015) 2399.
- [2] T. Takahashi *et al.*, Phys. Rev. E **62** (2000) 8606.
- [3] N. Sei and T. Takahashi, Sci. Rep. **7** (2017) 17440.

K. Shinoda and Y. Kobayashi<sup>1</sup>

*Department of Geosciences,  
Graduate School of Science, Osaka City University*

<sup>1</sup>*Research Reactor Institute, Kyoto University*

**INTRODUCTION:** The  $^{57}\text{Fe}$  Mössbauer spectroscopy have been widely used to analyses of  $\text{Fe}^{2+}/\text{Fe}^{3+}$  ratio and  $\text{Fe}^{2+}$  ratio between non-equivalent crystallographic sites of Fe bearing minerals. Fe ions in non-magnetic minerals such as olivine, pyroxene, mica show doublet peaks due to quadrupole splitting in Mössbauer spectra. The quadrupole splitting results from an interaction between the nuclear quadrupole moment and the electric field gradient (EFG) due to electrons around the nucleus. In general, while an  $\text{Fe}^{3+}$  ion occupying octahedral sites results in the quadrupole splitting as narrow as about 0.5mm/s, quadrupole splitting of  $\text{Fe}^{2+}$  results in the wider quadrupole splitting about 2mm/s. Mössbauer peaks have Lorentzian shapes, Lorentzian peaks are characterized by 4 variables, (1) isomer shift (IS), (2) quadrupole splitting (QS), (3) line width (LW) and (4) intensity ratio (IR). Doublet peaks of Mössbauer spectra are usually analysed by least square fitting (LSQ) raw data with allowing 4 variables to vary independently. Separation of doublet peaks due to  $\text{Fe}^{2+}$  and  $\text{Fe}^{3+}$  of mixed valence of iron minerals can be easily done, because wide QS of  $\text{Fe}^{2+}$  and narrow QS of  $\text{Fe}^{3+}$  do not overlap. Therefore, the most probable values of 4 variables can be converging, even if four variables are allowed to vary independently during LSQ. On the other hand,  $\text{Fe}^{2+}$  ions occupying two non-equivalent sites such as M1 and M2 sites in pyroxene give two kinds of doublet peaks of closely overlapping. In the measurements of Mössbauer spectra of thin sections of a single crystal, a constraint on the intensity ratio of quadrupole splitting is important during data fitting. Intensity ratio due to  $\text{Fe}^{2+}$  ( $\text{Fe}^{3+}$ ) occupying a crystallographic site can be calculated from an EFG tensor of the site. The determination of EFG tensor is important to calculate intensity ratio. To compare an experimentally determined EFG tensor with the crystal structure is important for theoretically calculating EFG tensors. The EFG tensor can be experimentally determined from intensity tensor measured by Mössbauer spectra of single crystal. Zimmermann (1975, 1983) proposed the formulation of EFG tensor from intensity tensor and an example of monoclinic crystal. In this study, Zimmermann's method was applied to aegirine

( $\text{NaFeSi}_2\text{O}_6$ ), in which  $\text{Fe}^{3+}$  occupies M1 site of pyroxene structure in order to determine EFG tensor of aegirine.

**EXPERIMENTS and RESULTS:** A single crystal of aegirine was used for this study. Six crystallographically oriented thin sections were prepared by measuring X-ray diffraction using precession camera. Thin sections #1 and #2 are normal to  $b^*$  and parallel to (110) cleavage plane, respectively, which are mounted on 1mm $\phi$  holed Al plate. Thin section #3 normal to  $a^*$ -axis was mounted on Goniometer and adjusted  $b^*$ -axis to dial (horizontal) direction by X-ray diffraction. Thin sections #4 and #5 normal to  $b^*$ -axis were mounted on Goniometer as  $c^*$  and  $a$ -axes to dial, respectively. Thin section #6 is normal to  $c^*$ -axis. In this study, Cartesian coordinate ( $X Y Z$ ) is set as  $X//c^*$ ,  $Y//a$ ,  $Z//b^*$  in order to set  $b$ -axis as  $Z$  and set  $a$ ,  $b$ ,  $c$ -axes as right-handed system, where  $a$ ,  $b$ ,  $c$  are real and  $a^*$ ,  $b^*$ ,  $c^*$  are reciprocal lattice vectors of aegirine. Mössbauer measurements were carried out in transmission mode on a constant acceleration spectrometer with an Si-PIN semiconductor detector (XR-100CR, AMPTEK Inc.) and multi-channel analyzer of 1024 channels. A 3.7GBq  $^{57}\text{Co}/\text{Rh}$  of 4mm $\phi$  in diameter was used as  $\gamma$ -ray source. An  $^{57}\text{Fe}$ -enriched iron foil was used as velocity calibrant. The two symmetric spectra were folded and velocity range was  $\pm 5\text{mm/s}$ . Thickness corrections of raw spectra were done by transmission integral method of Mosswin program. According to Zimmermann (1975, 1983), intensity and local EFG tensors is determined. As the results, three components of Electric Field Gradient (EFG) tensor of  $\text{Fe}^{3+}$  in M1 site of aegirine were (-0.218(5), 0.214(5), 0.004(10)). Asymmetric parameter  $\eta$  was nearly equal to 1. The principal axes of EFG tensor of aegirine are almost oriented to  $a^*$ ,  $b$ ,  $c$ -axes. While  $V_{xx}$  axis is determined to orient  $b$ -axis,  $V_{yy}$  and  $V_{zz}$  axes were not fixed along  $a^*$  or  $c$ -axes.

### REFERENCES

- Zimmermann, R. (1983) The intensity tensor formulation for dipole transitions (e.g.  $^{57}\text{Fe}$ ) and its application to the determination of EFG tensor. *Advances in Mössbauer spectroscopy* (Thosar, B.V. Ed.). pp.273-315, Elsevier Scientific Publishing Co. Amsterdam.
- Zimmermann, R. (1975) A method for evaluation of single crystal  $^{57}\text{Fe}$  Mössbauer spectra ( $\text{FeCl}_2 \cdot 4\text{H}_2\text{O}$ ). *Nuclear Instruments and Methods*. 128, 537-543.

T. Miura<sup>1</sup>, R. Okumura<sup>2</sup>, Y. Inuma<sup>2</sup>, S. Sekimoto<sup>2</sup> and K. Takamiya<sup>2</sup>

<sup>1</sup>National Metrology Institute of Japan, AIST

<sup>2</sup>Research Reactor Institute, Kyoto University

**INTRODUCTION:** National Metrology Institute of Japan (NMIJ) is responsible for developing certified reference materials and for establishing the traceability of SI (The International System of Units) on chemical metrology in Japan. To establish SI traceability, the primary method of measurements should be applied to the characterization of the certified reference materials. Recently, neutron activation analysis using comparator standard is recognized as a potential primary ratio method [1]. Despite the potential of neutron activation analysis as primary ratio method, the evaluation of the measurement uncertainty is required in any analysis. In general, there are three main components of uncertainty in neutron activation analysis, that is, sample preparation uncertainty, neutron flux homogeneity, and gamma ray measurement uncertainty. Usually, flux monitor is used to correct the neutron flux in-homogeneity. However, although the flux monitor can correct the neutron flux variation using the count rate of the known amount of the monitor nuclide, it does not reflect the neutron flux of the actual sample. The most practical method to eliminate neutron flux in-homogeneity and to improve gamma ray measurement uncertainty is an internal standard method [2-4]. For the development of primary inorganic standard solution as national standard, the purity of starting material has to be determined. The high purity Ti metal was candidate starting material for preparation of titanium standard solution as national standard of Japan. The several trace analytical methods including neutron activation analysis, were used for purity determination of the high purity Ti metal. In this study, we presented that capability of instrumental neutron activation analysis for determination of Cl, Br, and I in high purity Ti metal.

**EXPERIMENTS:** The high purity Ti metal was purchased from Sumitomo Metal Mining Co. Ltd. The informative purity value of the Ti metal was 99.9 %. The calibration solution of Cl was prepared from NMIJ primary standard solution. The In solution for the internal standard for Cl was prepared from NMIJ primary standard solution. The calibration solution of Br was prepared from NMIJ primary standard solutions. The Au solution for the internal standard for Br was prepared from a high purity metal.

The Iodine standard solution was prepared from NMIJ primary standard solution. The In solution for the internal standard for Iodine was prepared from NMIJ primary standard solution. Three hundred mg of the Ti metal samples were used for Cl and I analysis. On the other hands, one gram of Ti metal sample was used for Br analysis. The neutron irradiations were performed by KUR (Kyoto University Research Reactor) Pn3 (thermal neutron flux:  $4.7 \times 10^{12} \text{ cm}^{-2}\text{s}^{-1}$ ) for 15 min. For the determination of Br in the Ti metal samples, the neutron irradiation were performed using KUR TCPn (thermal neutron flux:  $8.0 \times 10^{10} \text{ cm}^{-2}\text{s}^{-1}$ , 12 h) for 12 h. The  $\gamma$  ray measurement system consisted of a Canberra GC4070-7500 Ge detector and a Laboratory Equipment Corporation MCA600

**RESULTS:** In this experiment, Cl, Br and I in the high purity Ti metal sample could not be detected even by using instrumental neutron activation analysis. Therefore, the upper limit of Cl, Br and I in the high purity Ti metal sample were estimated from the count rates of energy region of gamma rays emitted by each radioactive nuclide. The estimated upper limit of Cl, Br, and I were <1 mg/kg, <0.02 mg/kg and <0.1 mg/kg, respectively.

Impurity elements in high purity Ti metal sample were determined by multiple analysis methods such as instrumental neutron activation analysis, ICP-MS, combustion infrared spectrometry and so on. By subtracting the total value of impurity elements from 100%, the purity of the Ti metal sample was determined to be  $(99.973 \pm 0.0013) \%$ .

#### REFERENCES:

- [1] R.Greenberg, P. Bode, E. De Nardi Fernandes, *Spectrochim. Acta B*, **66** (2011) 193-241.
- [2] T. Miura, K.Chiba, T. Kuroiwa, T. Narukawa, A.Hioki, H. Matsue, *Talanta*, **82** (2010) 1143-1148.
- [3] T. Miura, H. Matsue, T. Kuroiwa, *J. Radioanal. Nucl. Chem.*, **282** (2009) 49-52.
- [4] T. Miura, R. Okumura, Y. Inuma, S. Sekimoto, K. Takamiya, M. Ohata, A.Hioki, *J. Radioanal. Nucl. Chem.*, **303** (2015) 1417-1420.

T. Takatsuka, K. Hirata, Y. Iinuma<sup>1</sup>, R. Okumura<sup>1</sup> and K. Takamiya<sup>1</sup>

National Metrology Institute of Japan, National Institute of Advanced Industrial Science and Technology

<sup>1</sup>Research Reactor Institute, Kyoto University

**INTRODUCTION:** Hafnium oxide is utilized as high-*k* dielectric films for semiconductor devices in order to attain the higher performance. The device fabrication process should be in precise control of the thickness of thin (typically a few nm) dielectric films. However, the accurate measurements of the thickness in length unit are getting laborious, possibly caused by the atomic fluctuation at the interface layers. We aimed to quantify hafnium in hafnium oxide films in weight unit, instead of in length, by means of isotope dilution-neutron activation analysis (ID-NAA) [1].

**EXPERIMENTS:** Hafnium oxide films were deposited on 4-inch Si wafers by magnetron sputtering. The target thickness was set to 4 nm. The homogeneity in thickness over the wafer was estimated less than 2% of standard deviation. The prepared wafers with the films were cut into 10 mm × 10 mm pieces for the measurements.

The procedure for ID-NAA has two sequences of an isotope dilution (ID) and a reverse-ID to ensure traceability to the SI units; the latter sequence was performed to determine the hafnium concentration in a spike solution by referring to a hafnium standard. The spike solution was prepared by dissolving <sup>174</sup>Hf-enriched hafnium oxide in a HNO<sub>3</sub> + HF aqueous solution, and by diluting to a proper concentration. For calibrating the amounts of hafnium, a working standard solution was prepared by diluting NIST SRM 3122 gravimetrically. For the ID analysis, small amounts of the spike solution was dropped onto each hafnium oxide sample using a polyethylene pipette (HfO<sub>2</sub>+Sp), while the spike solution or standard solution was dropped separately onto each piece of cleaned filter paper (Sp or STD), as shown in Fig. 1. The hafnium contents of the droplets were determined by weighing the polyethylene pipettes before and after every dropping. For the reverse-ID analysis, the spike and standard solutions were dropped onto one piece of filter paper (Sp+STD).

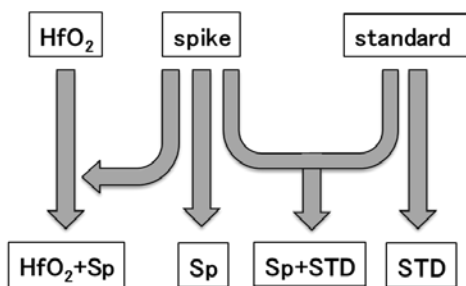


Fig. 1. Sample preparation for ID-NAA.

All the samples were sealed up separately in clean polyethylene bags, followed by being stacked in a polyethylene container for the neutron irradiation. The irradiation was performed for 4 hours with a  $5.5 \times 10^{12} \text{ cm}^{-2} \cdot \text{s}^{-1}$  thermal neutron fluence rate at Pn-2 in the Kyoto university research reactor (KUR). The gamma-ray activity of each sample was measured by a high-purity germanium detector (CANBERRA) with an energy resolution around 2.0 keV and a relative efficiency of 40% at 1333 keV.

**RESULTS:** As shown in Fig. 2, several peaks are found in the gamma-ray spectrum, and most of the large peaks were due to the hafnium isotopes generated during the neutron irradiation. The peaks at 343 keV and 482 keV were selected to calculate the gamma-ray intensity ratio of <sup>175</sup>Hf to <sup>181</sup>Hf for the samples. The integrated peak areas were converted into the counting rates at the end of the irradiation, taking into account of the radioactive decay and the dead time of the measuring system [2]. The amounts of hafnium in the hafnium oxide samples were calculated from the intensity ratios based on a formula reported in Ref. 1. The obtained amounts are 3.54 μg and 3.47 μg for two measured samples. Dividing the hafnium amounts by measured sample surface areas, the area densities are calculated to be 3.62 μg·cm<sup>-2</sup> and 3.58 μg·cm<sup>-2</sup>. The resultant average is 3.60 μg·cm<sup>-2</sup>, which agrees with the previous results of 3.68 μg·cm<sup>-2</sup> and 3.60 μg·cm<sup>-2</sup> obtained by NAA with an internal standards.

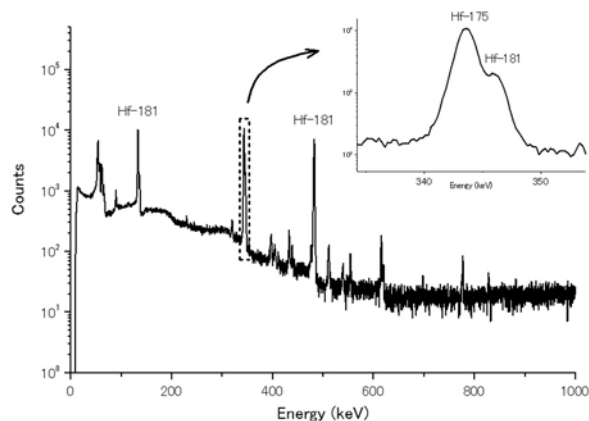


Fig. 2. Gamma-ray spectrum of hafnium oxide film + spike solution (HfO<sub>2</sub>+Sp).

#### REFERENCES:

- [1] C. Yonezawa *et al.*, *Anal. Chem.*, **55** (1983) 2059-2062.
- [2] G. Gilmore and J. D. Hemingway, *Practical gamma-ray spectrometry* (John Wiley & Sons, Chichester, 1995).

## CO12-5 The Structure of the DN-polymers under Different Temperature and Humidity

T. Tominaga, N. Sato<sup>1</sup>, R. Inoue<sup>1</sup> and M. Sugiyama<sup>1</sup>

Neutron Science and Technology Center, CROSS

<sup>1</sup> Institute for Integrated Radiation and Nuclear Science, Kyoto University

**INTRODUCTION:** Biocomposite systems have distinct hierarchical structures on the molecular, nanoscopic, microscopic, and macroscopic scales [1]. Synthetic materials polymerized from monomers are good mimics of biocomposites, and promise the creation of new materials.

We reported the fabrication of porous polymeric materials, namely, double-network polymers (DN-polymers) exhibiting unique mechanical properties against humidity change [2]. The DN-polymers were xerogels prepared from double-network hydrogels (DN-hydrogels) [3] consisting of two kinds of hydrophilic polymers with a crosslinker.

Previously we investigated static structures of dried-state DN-polymers by determining their porosity from nitrogen adsorption isotherms and mercury intrusion techniques. Besides, the morphologies of the DN-polymers were observed by scanning electron microscopy and laser microscopy. We showed that the DN-polymers formed a continuous porous network with diameters ranging from 1.7 nm to more than 100  $\mu\text{m}$  [4]. Three classes of hierarchical porous structure were identified. Small pores (diameter 1.7–10 nm) were present within the walls of mid-sized pores (diameter 60 nm), and the mid-sized pores resided in the walls of large pores (diameter 4  $\mu\text{m}$ ). Recently we also found that unique mechanical properties are not only room temperature but also temperature dependence. Therefore, we study the structure of the DN-polymers under temperature and humidity controlling atmosphere. The length scale  $\xi$  of  $3 < \xi \text{ nm} < 160$ , which covers a network of hierarchical structure more than approximately 20 nm and inside the first class of hierarchical structure composing a linear polymer chains less than approximately 20 nm is measured in this study using SAXS.

**EXPERIMENTS:** The samples were prepared by DN-hydrogels [3] from 2-acrylamido-2-methylpropane sulphonic acid sodium salt (NaAMPS) and acrylamide (AAm) crosslinked with N, N' -methylenebisacrylamide (MBAA). Sheet-shaped DN-hydrogels were frozen and dried in a freeze-dryer unit, yielding the sheet-shaped freeze-dried DN-polymers [2,4].

Flow-humidity controlling system was developed for this SAXS measurements by mixing dried and humid nitrogen gas. Sensirion humidity sensors were used for controlling and monitoring temperature and humidity. The temperature from 5 to 80 dC was controlling by a Partier system. we compared dried condition and a constant moisture concentration (approximately 0.05 g/cm<sup>3</sup>). Cu-SAXS (RIGAKU Nanopix) available at Institute for Integrated Radiation and Nuclear Science, Kyoto University was used.

**RESULTS:** Preliminary results are shown in Fig. 1. The SAXS profiles were divided by a profile at low temperature 5dC. Although details are not understood, these figures are clarified differences of tendencies between different humidity and temperature.

Compared to temperature dependence of wet and dried

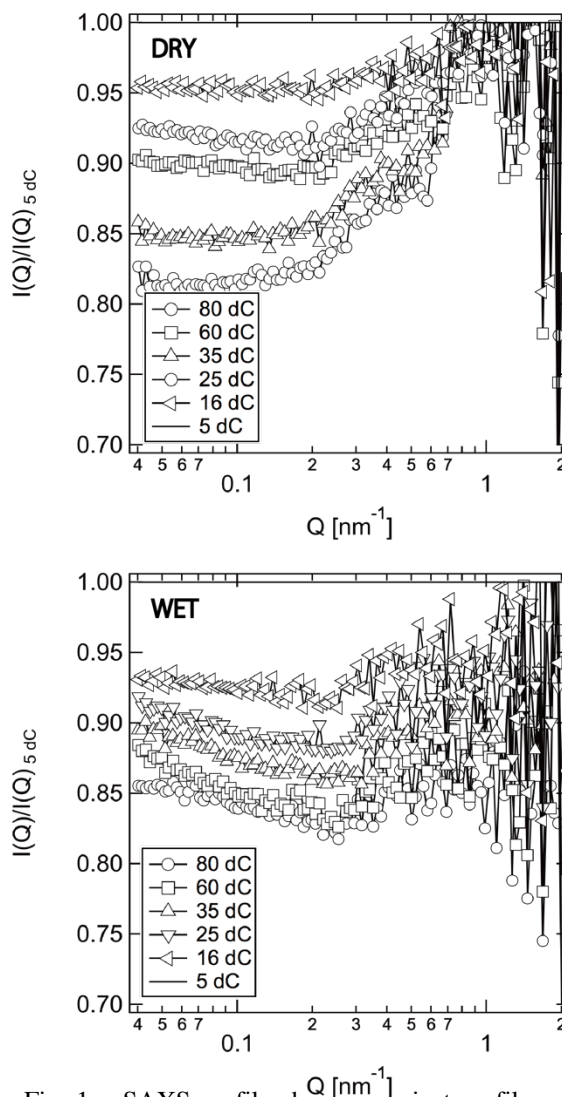


Fig. 1. SAXS profile changes against profiles of 5 dC under dried and wet conditions.

local structure of high-Q ( $>20 \text{ nm}$ ) is quite different. Under the dried state, the local structure is fixed, no structure change against temperature difference, however under the wet state, the local structure can expand with a kind of similarity. This indicates that the mobility of inner structure of the first hierarchical structure composing a linear polymer chains against humidity is quite different. Further careful analysis would be required.

### REFERENCES:

- [1] B.-L. (Editor) Su, C. Sanchez, X.-Y. (Editor) Yang, eds., *Hierarchically Structured Porous Materials*, (Wiley-VCH Verlag GmbH & Co. KGaA, Weinheim, 2011.)
- [2] T. Tominaga *et al.*, ACS Macro Lett. **1** (2012) 432–436.
- [3] J.P. Gong *et al.*, Adv. Mater. **15** (2003) 1155–1158.
- [4] T. Tominaga *et al.*, Polymer **108** (2017) 493e501

## CO12-6 Electron Induced Noise on Avaranche Photodiode for Ganymede Laser Altimeter of Jovian Icy Satellite Exploerer

M. Kobayashi, O. Okudaira, M. Fujii<sup>1</sup>, T. Takahashi<sup>2</sup> and N. Abe<sup>2</sup>

*Planetary Exploration Research Center, Chiba Institute of Technology*

<sup>1</sup>*FAM science Co., Ltd.*

<sup>2</sup>*Research Reactor Institute, Kyoto University*

**INTRODUCTION:** The Ganymede Laser Altimeter (GALA) as part of the JUICE (Jovian Icy Satellite Explorer) payload is one of the instruments focusing on aspects related to the presence and characterizations of subsurface water oceans [1][2]. For the first time the time-variability of the global figure of a moon due to tides exerted by Jupiter will be detected by altimetry measurements.

GALA is a laser ranging instrument that measures time-of-flight of a transmitted laser pulse from the instrument on the spacecraft and the returned pulse from the surface of Ganymede. The returned laser pulse must consist of tiny amount of photons and high sensitive optical sensor is required to be used for light detection. The returned laser pulse reflects terrain slope and flatness, therefore the shape of the returned pulse is needed to be measured and recorded. In case of GALA, the receiver unit consists of a telescope, a back-end optics unit, an optical sensor, an analog electronics module and a range finder module. For optical sensor and the front-end electronics, we adopted an optical receiver module which contains an avalanche photo diode (hereafter APD) and a trans-impedance amplifier as front-end electronics in one package, which is manufactured by Excelitas Technologies, Montreal in Canada. The APD module is customized for our purpose based on one of their commercial APD modules, LLAM-1060-R8BH.

In case of GALA, we use the APD as an optical sensor converting optical return pulse to electrical signal while the APD is also sensitive to incident ionizing radiation. Ionizing radiation can induce hole-electron pairs in the depression layer of APD and the APD outputs electrical signal. Induced signals by ionizing radiation in orbit may affect light detection as false signals, called radiation noise. Jupiter has a strong magnetosphere and previous studies revealed that energetic electrons are trapped in the magnetosphere and major component among the other ionizing radiation like proton and the other energetic ion. The APD will be shielded up against to the Jovian radiation environment however some of electrons can penetrate the shield into the APD.

In this study, we used KURRI-LINAC as an electron beam source to emulate electrons irradiating the APD to investigate how energetic electron induces signals and interferes the returning laser pulse signal.

**EXPERIMENTS:** As device under test, we used an engineering module (EM) of APD module customized for GALA (GALA APD). The EM has the same performance as the flight module of GALA APD but before quality conformance inspection test for JUICE environment condition.

We performed twenty one runs of the LINAC and electrons was accelerated to six different energies for irradiation to the DUT, 5, 10, 20, 30 and 40 MeV. Irradiation angle is changed to be 0° (straight forward), 30°, 45°, 60°, 90° (right beside) and 180° (backward). The output signals of the trans-impedance amplifier in APD module were recorded with a digital oscilloscope.

**RESULTS:** Incident electron on the APD sensor induces a signal of short pulse, typically both rise and fall time are 2nsec. The pulse shape is not changed by the incident electron energy while the pulse shape is slightly broaden when the incident angle is large, 2-3nsec for incident angle of 60deg.

Pulse height of the signal induced by electrons has variation ranging 150 mV to higher when the responsivity of the APD sensor is about 700kV/W. For any energies and incident angles of electrons, the most events of the induced signal has pulse heights of 150mV to 300mV.

For backward irradiation, the APD module as DUT does not output any signals induced by irradiated electrons when the electron energy is 5MeV or lower. Apparently a structure on the back of the APD sensor in the module shields against incoming radiation.

**CONCLUSIONS:** We conclude that radiation induced noise on GALA APD in orbit does not significantly affect the performance of GALA. We will have radiation induced noise on GALA APD signal in orbit, however, the rate of occurrence is low (the incident rate of electron hit on the APD sensor is low), and the radiation induced noise hardly degrade SNR of the stop pulse because the pulse shape is different from the stop pulse rather similar to the start pulse. If a radiation induced noise has larger pulse height than power supplies voltages, it affect the signal baseline to be unstable but the radiation induced noise does not have such large pulse height as that.

### REFERENCES:

- [1] H. Hussmann *et al.*, European Planetary Science Congress 2017, held 17-22 September, 2017 in Riga Latvia, **11** (2017) id. EPSC2017-567.
- [2] H. Hussmann *et al.*, 19th EGU General Assembly, EGU2017, proceedings from the conference held 23-28 April, 2017 in Vienna, Austria., **19** (2017) 16366.

M. Aoki, N. Abe<sup>1</sup>, F. Morimoto<sup>2</sup>, D. Nagao, Y. Nakatsugawa<sup>3</sup>, H. Natori<sup>4</sup>, T.M. Nguyen<sup>5</sup>, Y. Seiya<sup>2</sup>, T. Takahashi<sup>1</sup>, N. Teshima<sup>2</sup> and K. Yamamoto<sup>2</sup>

*School of Science, Osaka University*

<sup>1</sup>*Research Reactor Institute, Kyoto University*

<sup>2</sup>*Faculty of Science, Osaka City University*

<sup>3</sup>*Institute of High Energy Physics, China*

<sup>4</sup>*Institute for Basic Science, Korea*

<sup>5</sup>*University of Science and Technology Da Nang City*

**INTRODUCTION:** There has been no observations related to a charged-lepton flavor violation (CLFV) process such as  $\mu \rightarrow e \gamma$ ,  $\mu$ -e conversion,  $\tau$ -CLFV decays and so on up to now. Based on this fact, the charged-lepton flavor is assumed to be conserved a priori in the Standard Model of particle physics (SM). However, it is rather natural not to be conserved in most of the models beyond SM (BSM). Any discoveries or improvements of the upper limit on the branching ratio of CLFV processes provide very important information to BSM. DeeMe is one of experiments that aim to search for CLFV with  $\mu$ -e conversion in nuclear field [1]. It uses high-power high-purity pulsed proton beam from J-PARC RCS. The detector of DeeMe should be operational after  $\mathcal{O}(\mu\text{s})$  from a burst of particles (100 GHz/mm<sup>2</sup>). We successfully developed such a detector with high-voltage switching technique [2]. It is very important to evaluate the performance of the detector before we start the physics data taking at J-PARC MLF.

**EXPERIMENTS:** Measurement of detection efficiency for the newly developed DeeMe detector was performed at KURRI. Figure 1 shows the experimental setup placed at the exit of the electron LINAC at KURRI. The beam size was shaped to 2 cm  $\times$  2 cm by a collimator, and the high-voltage switching multi-wire proportional chamber (MWPC) was placed in between two plastic-scintillation counters (TC1 and TC2). The timing of the MWPC high-voltage switch was synchronized to the electron gun timing (25 Hz) so that the MWPC is sensitive to the coming charged particles only during 6

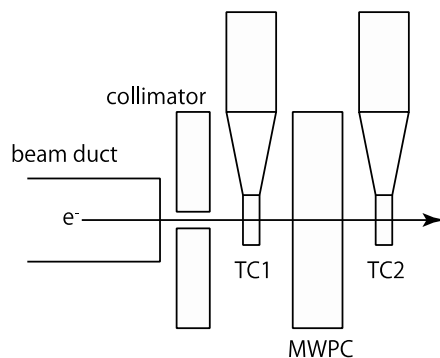


Fig. 1 Experimental Setup

$\mu\text{s}$  in every 40 ms. A heater voltage of the electron gun of the LINAC was adjusted to reduce the number of electrons hitting the MWPC being only a few per pulse. Signal waveforms from MWPC were recorded with Fast ADCs. Signals from TC1 and TC2 were also recorded with another Fast ADC. Waveform data were obtained with several different conditions of the electron gun timings and electron intensities.

In the off-line analysis, the recorded waveforms from TC1 and TC2 were scanned to find hits in coincidence. In the case that there was the coincidence hit in TC1 and TC2, the waveforms from MWPC were scanned to find the hits at the same timing. The MWPC efficiency was calculated by taking a ratio between the number of MWPC hits and that of the TC1-TC2 coincidence hits.

**RESULTS:** Figure 2 shows the efficiency as a function of hit timing. The efficiency of this high-voltage switching MWPC is more than 98% after 1.3  $\mu\text{s}$  from the gate of the high-voltage switching. This efficiency is sufficiently high as a charged-particle detector for DeeMe experiment.

Mode24.Paget (DeeMe.02.Reconstruction)

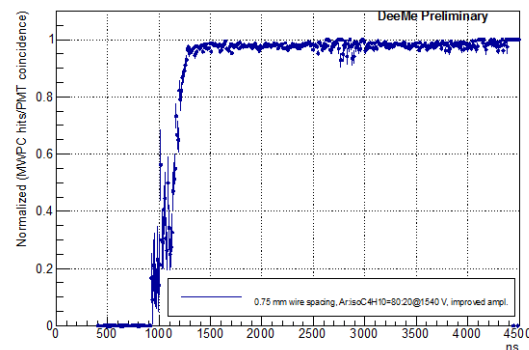


Fig. 2 Efficiency of the high-voltage switching MWPC as a function of time. Time origin corresponds to the time of high-voltage gate.

### REFERENCES:

- [1] N. Teshima on behalf of the DeeMe Collaboration, "DeeMe experiment to search for muon to electron conversion at J-PARC MLF", in proceedings of NUFACT conference PoS (NuFact2017) 109 (2018).
- [2] H. Natori, et al., "A fast high-voltage switching multiwire proportional chamber", Prog. Theor. Exp. Phys. 2017(2) 023C01 (2017).

## Influence of Submerged Condition and Soil on the Cadmium and Arsenic Concentration of Brown Rice

T. Inamura, D. Tojou, S. Fukutani<sup>1</sup> and K. Takamiya<sup>1</sup>

*Graduate School of Agriculture, Kyoto University*

<sup>1</sup>*Institute for Integrated Radiation and Nuclear Science, Kyoto University*

**INTRODUCTION:** Cadmium and arsenic concentration of brown rice are influenced by submerged condition of a paddy field which paddy rice grew. However, the Cd and As concentration of brown rice fluctuate by the growth environment except the submerged condition [1]. We examined the influence of the submerged condition to the Cd and As concentration of brown rice using the different paddy field soil.

**EXPERIMENTS:** The “Senshou” cultivar, which is Tropical-Japonica and upland rice, was used in this study. The soil (a) with the high concentration of Cd and As and the soil (b) with the low those concentration were used for cultivation of the upland rice. Four submerged treatments were carried out: treatment 3 (always keeping flooded) to treatment 0 (always keeping no flooded). The brown rice gathered at maturity stage was dried at 70°C for 48 h. The dried brown rice was crushed with an agate mortar, and the crushed sample was digested by microwave digestion. The Cd and As concentration of the digested solution of brown rice was determined using inductively coupled plasma-mass spectrometry (ICP-MS).

**RESULTS:** Influence of submerged condition and soil on the cadmium and arsenic concentration of brown rice are shown in Fig. 1. The Cd and As concentration in brown rice were influenced by those concentrations in the soil regardless of intensity of submerged treatment. The tendency that Cd concentrations increased and As concentration decreased when flooding strength decreased was detected in both soil. These results indicated that the submerged condition is able to be estimated by two-dimensional distribution of the Cd and As concentration of brown rice regardless of the both concentration of paddy soil.

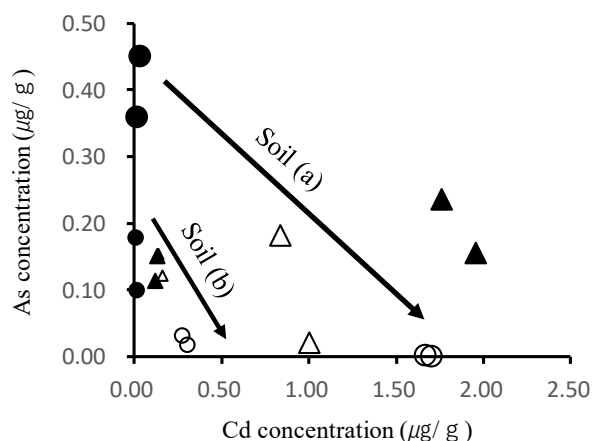


Fig. 1, Influence of submerged condition and soil on the cadmium and arsenic concentration of brown rice.

●, ▲, △ and ○ indicate the submerged treatment levels of 3 (always keeping flooded), 2, 1 and 0 (always keeping no flooded), respectively.

### REFERENCE:

[1] T. Inamura *et al.*, *Jap. J. Crop Sci.*, **75** (2006) 273-280.

T. Kubota, S. Fukutani, Y. Shibahara and T. Ohta<sup>1</sup>

*Institute for Integrated Radiation and Nuclear Science,  
Kyoto University*

<sup>1</sup>*Central Research Institute of Electric Power Industry*

**INTRODUCTION:** Radioactive tracers are a useful tool for the investigation on the fate and migration of various elements in the environment [1]. In particular carrier free radionuclides, without naturally occurring isotopes, are important for the study on the migration of trace elements in living organisms without any chemical toxicity. Carrier free tracers can be produced through ( $\gamma$ , p) reaction. In this report we produced the radioactive tracers ( $^{43}\text{K}$  and  $^{136}\text{Cs}$ ), which are planned to be applied for the investigation on the migration of potassium and  $^{137}\text{Cs}$  in glasses and trees.

**EXPERIMENTS:**  $^{43}\text{K}$  and  $^{136}\text{Cs}$  were produced from calcium and barium, respectively. Target materials used were calcium chloride dihydrate and barium chloride dihydrate. Each material was dried up in a quartz test tube and then encapsulated in quartz under vacuum. The sample material was irradiated with high-energy photons, which was generated by the bombardment of Pt with electrons of 30 MeV, for 20 hours at the KURRI-LINAC [2]. Potassium and cesium were purified by a carbonate precipitation method from the target sample immediately after irradiation. The target sample was dissolved with  $\text{H}_2\text{O}$  and the resulting solution was equally divided into two polyethylene centrifugation tubes. This solution was added with 3 M ammonium carbonate to remove calcium and barium as precipitate [3]. After centrifugation the supernatant was transferred to a glass beaker and heated to dryness in order to remove  $\text{HN}_4\text{Cl}$ . Finally,  $^{43}\text{K}$  and  $^{136}\text{Cs}$  were dissolved into 1 M HCl.

**RESULTS:** Target materials, calcium and barium, were sufficiently removed by the precipitation method in Fig. 1 and 2. This method showed that the recovery ratio and decontamination factor of alkali metal was 0.9 and  $10^5$ , respectively. From the calcium target strontium as impurity and  $^{47}\text{Sc}$  as decay product of  $^{47}\text{Ca}$  were also removed. In the barium target  $^{129}\text{Cs}$  produced simultaneously was one of major gamma emitters; however, this nuclide can be ignored after cooling for 2 weeks due to its short half-life of 1.34 d. The induced radioactivity of other cesium nuclides,  $^{132}\text{Cs}$ ,  $^{134}\text{Cs}$ , and  $^{137}\text{Cs}$ , was low enough not to disturb radioactivity measurements. Radioactive tracers,  $^{43}\text{K}$  and  $^{136}\text{Cs}$ , suitable for in vivo experiments were produced and will be applied for plant and animal experiments in future work.

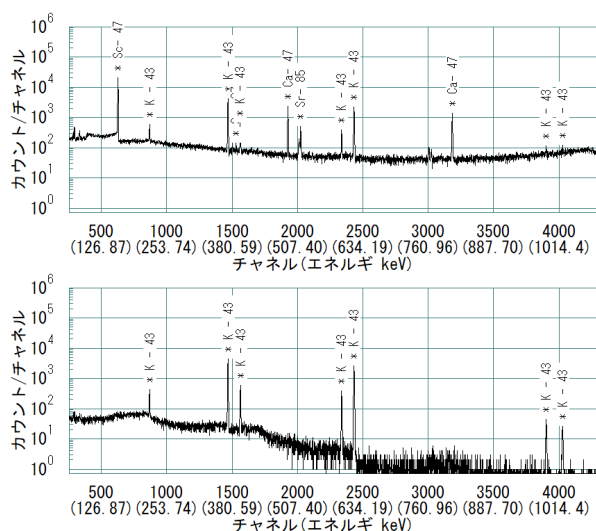


Fig. 1. Gamma-ray spectra of  $^{43}\text{K}$  before (upper) and after (lower) purification.

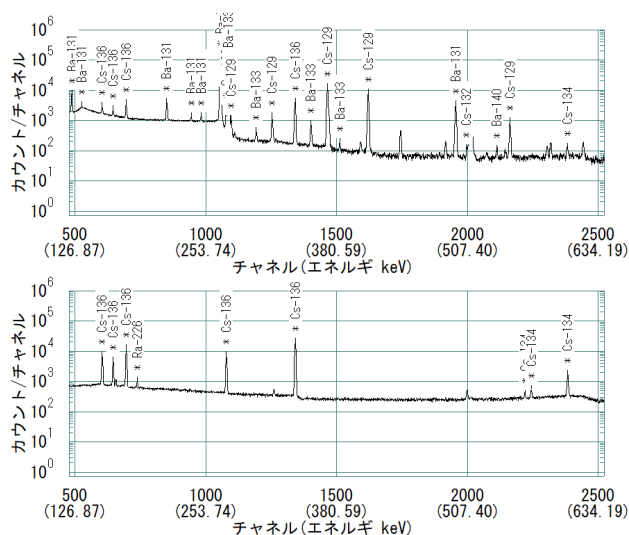


Fig. 2. Gamma-ray spectra of  $^{136}\text{Cs}$  before (upper) and after (lower) purification.

#### REFERENCES:

- [1] T. Kubota *et al.*, J. Radioanal. Nucl. Chem. **296** (2013) 981-984.
- [2] T. Kubota *et al.*, KURRI Progress Report 2011 (2012) 286.
- [3] T. Kubota *et al.*, KURRI Progress Report 2016 (2017) 19.

H. Masui, A. H. Kafi, J. C. Javier, T. Tumenjargal,  
M. Cho and K. Takamiya<sup>1</sup>

*Laboratory of Spacecraft Environment Interaction Engineering, Kyushu Institute of Technology*

<sup>1</sup>*Research Reactor Institute, Kyoto University*

**INTRODUCTION:** Kyushu Institute of Technology (Kyutech) has been developing nano satellites since 2010. Kyutech's main concern is the environmental testing. As a part of environmental testing, the radiation testing is also important. Since 2012, Kyutech has tested the radiation test using  $^{252}\text{Cf}$  in Kyoto University Research Reactor Institute. Currently, Kyutech are developing many cubesats and a standard bus system. The development of standard bus system has many advantages such as improvement of reliability, short delivery and the achievement of mission-oriented satellite development. For the next generation bus system, Kyutech suggest a back plane type configuration<sup>[1]</sup>. To improve the accessibility and flexibility of backplane type configuration, we decided to introduce Complex Programmable Logic Device (CPLD) as a new device to back plane. The advantage of CPLD is that the signal wiring can be changed by changing the program without changing the hardware. Field Programmable Gate Array (FPGA) also has the same characteristics as CPLD, but it differs from FPGA in that the power consumption of CPLD is small. The CPLD will be installed to cubesat project of BIRDS-3 and will be demonstrated on orbit. The backplane installed CPLD needs a high reliability because the backplane needs to operate without error until deorbiting. The purpose of this test is to evaluate the tolerance of CPLD for SEE. This document reports the detail of testing and test results of CPLD.

**EXPERIMENTS:** Figure 1 shows the experimental setup. Two CPLDs were installed to vacuum chamber at the same time and a total four CPLDs were tested. A model number of CPLD tested was LC4256ZE5TN144C manufactured by Lattice Semiconductor,. Inputs and outputs of the CPLD are connected each other and its functions are confirmed by sending and receiving data between the input and the output. The data transferring was checked with a serial communication of RS232 via PC. Figure 2 shows the CPLD tested. The package of CPLD was removed for the heavy ion exposure from  $^{252}\text{Cf}$  source.  $^{252}\text{Cf}$  source was mounted on XYZ stage and the position of  $^{252}\text{Cf}$  was controlled from outside and was moved above CPLDs. In the test, Single Event latch-up (SEL) current was also measured by oscilloscope and digital acquisition (DAQ).

**RESULTS:** Table 1 shows the summary of test results for four CPLDs. A nominal current of CPLD is 7 mA. When SEL occurs, increasing current consumption was observed in all CPLDs. Although SEL was observed, the function of CPLD as data transferring was never lost. The

maximum SEL current was 37mA for all samples, and no difference was observed with respect to the maximum SEL current. However, in term of the probability of SEL occurrence, a large difference was observed. Especially, there was a big difference between sample 2 and 4. Improvement of statistical performance by longer test will be a future subject. From the viewpoint of satellite system, the characteristic that CPLD does not hang even when SEL occurs is very important. However, whether to take measures against current increase should be discussed because the current increasing due to SEL of the CPLD is much smaller than that of typical microprocessors and the implement of reset system for the CPLD induces the complexity of system.

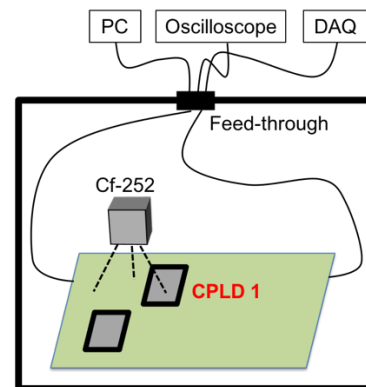


Fig. 1 Test setup

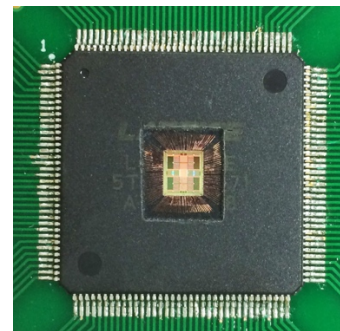


Fig. 2 Test article (CPLD decapped)

Table 1 Summary of test results

CPLD sample ID	Exposure time, hr	Number of SEL, -	Range of SEL current, mA
1	2	4	17 to 34
2	1	5	18 to 34
3	2	6	19 to 34
4	1	1	34

**REFERENCE:**

[1] S. Busch *et al.*, The 4S Symposium (2016).

# CO12-11 Growth of Adsorbed Additive Layer for Further Friction Reduction Confirmed by Multi-Analytical Methods Including Neutron Reflectometry

T. Hirayama, Y. Sasaki<sup>1</sup> and M. Hino<sup>2</sup>

Dept. of Mechanical Eng., Doshisha University

<sup>1</sup>Dept. of Mechanical Eng., Graduate School of Doshisha University

<sup>2</sup>Institute for Integrated Radiation and Nuclear Science, Kyoto University

**INTRODUCTION:** Understanding the state of the boundary lubrication layer formed by additive molecules and its role is an important research topic because the formation of a boundary layer greatly affects the coefficient of friction under boundary lubricated conditions. Typical models of the boundary lubrication layer are Hardy's monolayered model and Allen's multilayered model, and the conflict between them has resulted in a 'monolayer-multilayer controversy'. Actually, the most important issue is boundary layer sustainability, so the formation model, monolayer or multilayer, may be not so important. However, for a deeper understanding of the formation process, obtaining information on the actual interface is quite useful. Recent advances in interfacial analyzers have enabled physical/chemical information related to the structure of the boundary layer to be obtained through various *in-situ* analyses. This report shows the 'growing' behaviour of an adsorbed additive layer onto metal surface due to high pressure by means of NR with in conjunction with the result obtained through cross-sectional imaging by FM-AFM we already published before [1]. It also discusses the relationship between the structure of the adsorbed layer and its coefficient of friction as measured by AFM with a SiO<sub>2</sub> colloidal probe.

**EXPERIMENTAL RESULTS:** The reflectivity profiles from the target interface are shown in Figure 1. The substrate we selected was Cu-coated Si block. The profiles in PAO (bottom) were drawn with decoupling for the profile in PAO with deuterated palmitic acid (d-PA) (middle) and with centuplicating for profile in PAO with d-PA at 3.0 MPa (top) for clear viewability, though the maximum values of reflectivity in all of original profiles were 1. The optimum fitting lines based on Parratt's theory are also shown. In comparison of reflective profiles for PAO (bottom) and PAO with d-PA (middle), the reflectivity profiles are obviously slightly different: the fringe interval in the profile for PAO with d-PA is clearly narrower than in the profile for PAO. Fitting based on Parratt's theory showed that the adsorbed additive layer on the Cu surface was about 1.4 nm thick and that the density of the additive in the layer was almost the same as that of pure deuterated palmitic acid. It means that a monolayer of palmitic acid molecules was formed on the Cu surface with high grafting density which is almost the same as that of pure palmitic acid. In addition, further fitting operation revealed that the

thickness the adsorbed additive layer grew up to be 5.9 nm under high pressure. These results suggest that using high pressure can make the additive layer thicker.

The coefficients of friction measured with the colloidal probe AFM under various loads are shown in Figure 2. It shows that when pure hexadecane was used, the coefficient of friction was 5% lower after pre-scratching than in the non-scratched area because the surface was made smoother by the pre-scratching due to the running-in effect. When hexadecane with palmitic acid was used, on the other hand, the coefficient of friction was 12% lower after pre-scratching than in the non-scratched area even though the running-in effect became smaller than that in the case without palmitic acid because the surface profile in area A did not change. This higher reduction ratio of coefficient of friction for the case with acid is expected to be caused by the change in additive layer formation due to the pre-scratch treatment. These results and those of the previous structural analysis show that an adsorbed layer easily grows into a multilayer under tribological conditions and that the growth of the layer contributes more greatly to a reduction in the coefficient of friction.

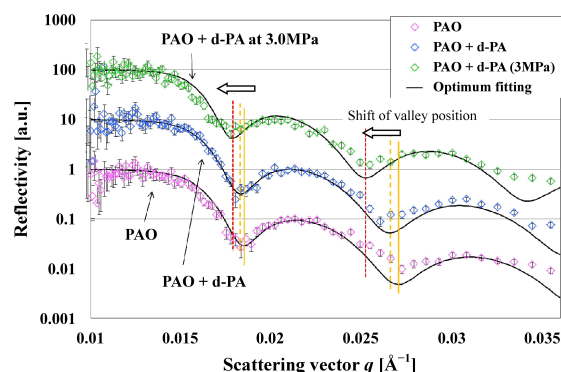


Fig. 1 Reflectivity profiles obtained from the interface in PAO (bottom), in PAO with deuterated palmitic acid (d-PA) (middle), and in PAO with d-PA at 3.0 MPa (top).

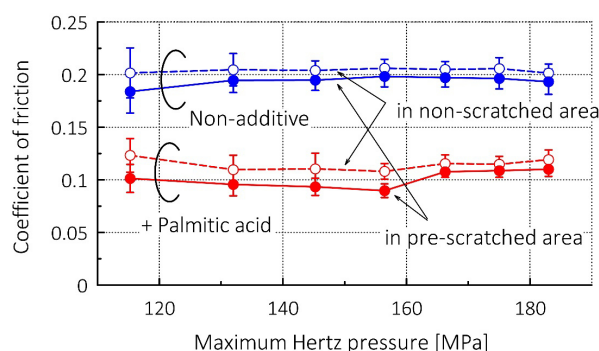


Fig. 2 Coefficients of friction measured with SiO<sub>2</sub> colloidal probe in hexadecane without/with palmitic acid in pre-scratched area and outside area.

## REFERENCE:

[1] T. Hirayama *et al.*, *Lungmuir*, **33(40)** (2017) 10492.

T. Miyazawa and Y. Tanaka<sup>1</sup>

School of Materials and Chemical Engineering, Tokyo Institute of Technology

<sup>1</sup>Department of Metallurgy and Ceramics Science, Tokyo Institute of Technology

**INTRODUCTION:** A lot of studies of precipitation phenomena in metallic materials for increasing a strength and stability of microstructure were carried out with TEM (Transmission electron microscope) observation. On the other hand, recently, small angle X-ray scattering (SAXS) method with using synchrotron X-ray has been received attention as an investigation method of the precipitates dispersed in the metallic materials[1,2]. The SAXS profiles can be analyzed the size and shape of precipitates. However, most studies about metallic materials with SAXS method assumed the precipitate shape is sphere. Only the size of precipitates was estimated from the SAXS profiles. In this study, both of the shape and size of precipitates in Cu alloys aged for various conditions were estimated to investigate the usability of the SAXS measurement.

**EXPERIMENTS:** The specimens were cut from plates of a Cu-2.15mass%Ni-0.49mass%Si alloy and Cu-1.31mass%Co-0.69mass%Fe alloy. These specimens were solution-treated at 1323 K for 1 h, quenched into water. After that, Cu-Ni-Si alloy specimens were aged at 973 K and Cu-Co-Fe alloy specimens were aged at 923 K for various times. After aging, Ni<sub>2</sub>Si particles having ellipsoidal shape and CoFe particles having flattened rectangular shape are dispersed in Cu matrix, respectively[3,4]. Thin foils for SAXS measurement about 200 μm thickness were prepared from these aged specimens by mechanical polishing. The SAXS measurements were carried out in BL19B2 at SPring-8. That beam line has the two measurement conditions such as the SAXS with camera length equal to 3.1 m and the USAXS (Ultra SAXS) with the camera length equal to 41.6 m to acquire wide  $q$  range scattering profiles. The incident X-ray energy is 30 keV.

**RESULTS:** Figure 1 shows the scattering profiles measured from the Cu alloy specimens. All scattering profiles are constituted of SAXS and USAXS profiles. The profiles acquired from as-quenched specimens indicate the decrease as a function of scattering vector  $q$ . The SAXS profiles from ellipsoid and rectangular particles has the broadening shoulder which is proportion to  $q^{-3}q^{-1}$ [5]. Convex shoulder parts exist on scattering profiles measured from the aged specimens. The convex shoulders are shifting from low  $q$  region to high  $q$  region and broadening with increasing the aging time in Cu-Ni-Si alloy. That means the size and shape anisot-

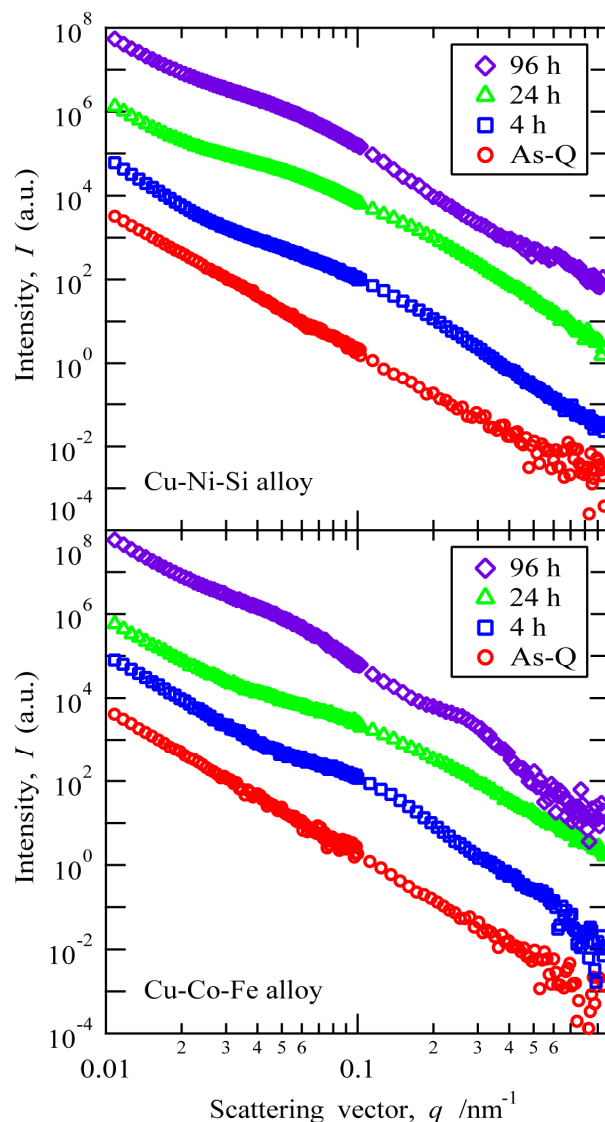


Fig. 1. The scattering profiles of Cu-Ni-Si alloy and Cu-Co-Fe alloy.

ropy of the Ni<sub>2</sub>Si particles increases with the increase of aging time. Similarly, in Cu-Co-Fe alloy, the convex shoulders move from low  $q$  region to high  $q$  region with increasing the aging time and shoulder broaden occurs. The CoFe particles also grow and the shape anisotropy changes with the increase of aging time.

#### REFERENCES:

- [1] Y. Takahashi, *et al.*, Mater. Trans., **48** (2007) 101-104.
- [2] Y. Oba, *et al.*, ISIJ International, **52** (2012) 457-463.
- [3] C. Watanabe, R. Monzen, J. Mater. Sci., **46** (2011) 4327-4335.
- [4] C. Kanno, *et al.*, Phil. Mag. Let., **90** (2010) 589-598.
- [5] J. S. Pedersen, Adv. Col. and Inter. Sci., **70** (1997) 171-210.

Y. Yanagisawa, T. Chatake<sup>1</sup>, T. Saito<sup>1</sup>, K. Morishima<sup>1</sup>, R. Inoue<sup>1</sup> and M. Sugiyama<sup>1</sup>

Faculty of Pharmaceutical Sciences, Chiba Institute of Science

<sup>1</sup>Institute for Integrated Radiation and Nuclear Science, Kyoto University

**INTRODUCTION:** Natto is a Japanese traditional fermented food made from soybeans by *Bacillus subtilis natto*. *Bacillus subtilis natto* produces various biologically active substances, which contribute to health. In addition, *Bacillus subtilis natto* is one of high-resistance bacteria. We took two biophysical approaches to *Bacillus subtilis natto*; structural study of macromolecular complexes containing vitamin K<sub>2</sub>, and irradiation study of *Bacillus subtilis natto*.

(1) Although vitamin K<sub>2</sub> is water-insoluble, *Bacillus subtilis natto* produces a large amount of water-soluble macromolecular complex containing vitamin K<sub>2</sub> (hereafter natto-MK-7). While natto-MK-7 is already commercially available as supplement, its structural information is poor. In the present study, natto-MK-7 was investigated through the combination of size-exclusion chromatography and dynamic light scattering (SEC-DLS), which was developed at Institute for Integrated Radiation and Nuclear Science, Kyoto University (KURNS).

(2) *Bacillus subtilis natto* takes two states; spores and vegetative cells. So far, it is well known that the spores has high radiation resistivity. In the present study, radiation resistivity of vegetative cells were measured using Co-60 gamma-ray at Co-60 Gamma-ray Irradiation Facility of KURNS.

**EXPERIMENTS:** (1) *Bacillus subtilis natto* was cultured in liquid medium. The cultured medium was centrifuged to remove precipitants, and its supernatant was concentrated by ultracentrifuge membrane. Natto-MK-7 was isolated from the concentrated medium. The repetition of ion-exchange chromatography was carried out to obtain purified natto-MK-7. SEC-DLS was carried out using HiPrep 16/60 Sephacryl S-300 HR on AKTA prime FPLC system and a system consisting of a 22 mW He-Ne laser ( $\lambda = 632.8$  nm), an avalanche photodiode mounted on a static/dynamic compact goniometer, ALV/LSE-5003 electronics and an ALV-5000 correlator.

(2) Glycerol stock of the clone *Bacillus subtilis natto* was pre-incubated overnight, and was inoculated in LB medium. After a few hour, 600-nm optical density (OD<sub>600</sub>) of the medium reached in the range of 0.4~1.0. The medium was centrifuged with 1,000 g for 10 minutes. After centrifugation, the supernatant was removed, then the precipitant was suspended in PBS(-) buffer. Seven samples were prepared, and irradiated with gamma rays at a dose of 0, 25, 50, 75, 100, 200, and 400 Gy at a dose rate of 24 Gy/min. After the irradiation, each liquid medium was diluted by PBS(-) medium, and plated. Colony forming units were counted after 6-hour incubation at

42 °C.

**RESULTS:** (1) As shown in Fig. 1, the chart of size-exclusion chromatography was clarified from SEC chart (refer to Fig. 1(a)). The frequencies of decay time from Fr. 1 and Fr. 4, which were purified from SEC are shown in Fig. 1 (b). The peak hydrodynamic radii from Fr.1 is much larger than that evaluated from monomeric form of natto-MK-7. On the other hand, natto-MK-7 mainly possesses the monomeric form in Fr. 4. It can be concluded that SEC-DLS contributes to observe pure monomeric form of natto-MK-7 having polymeric forms in nature.

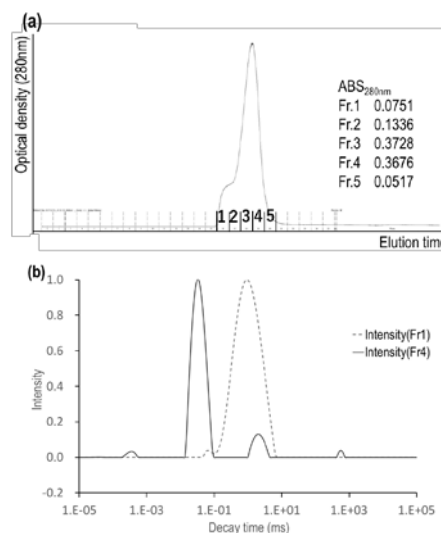


Fig. 1. The result of SEC-DLS of natto-MK-7. (a) The SEC chart, (b) the particle-size distribution of the Fr. 1 and 4, respectively.

(2) Fig. 2 shows the survival fraction curve of *Bacillus subtilis natto* against Co60-gamma ray. In this experiment, *Bacillus subtilis natto* shows radiation resistivity to low radiation dose (0~50 Gy), and an exponential decay of survival fraction was observed after 50 Gy dose. The resistivity to low radiation dose observed in this irradiation experiment is larger than those observed in *E. Coli* in previous studies. On the other hand, the exponential decay is comparable with those of *E. Coli*. Further experiments are necessary to confirm the present results.

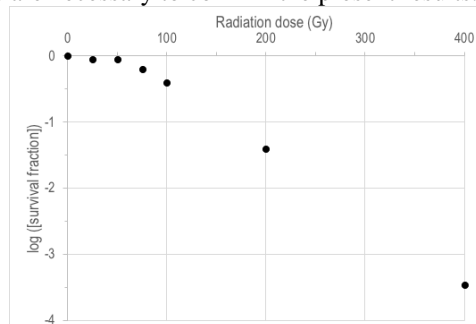


Fig. 2. The radiation survival fraction curve of *Bacillus subtilis natto*.